The Astrophysical Journal, 860:80 (11pp), 2018 June 10 https://doi.org/10.3847/1538-4357/aac2ba

Twisting/Swirling Motions during a Prominence Eruption as Seen from *SDO*/AIA

V. Pant[1], A. Datta[1,2], D. Banerjee[1,3], K. Chandrashekhar[1,4], and S. Ray[5]
[1] Indian Institute of Astrophysics, Bangalore 560 034, India; vaibhav@iiap.res.in, vaibhavpant55@gmail.com
[2] HKBK College of Engineering, Bangalore 560 045, India
[3] Center of Excellence in Space Sciences, IISER Kolkata, India
[4] Shandong Provincial Key Laboratory of Optical Astronomy and Solar-Terrestrial Environment, Institute of Space Sciences, Shandong University, Weihai, 264209 Shandong, People's Republic of China
[5] Department of Physics, Jadavpur University, Kolkata 700032, India
Received 2016 November 29; revised 2018 April 27; accepted 2018 April 27; published 2018 June 14

Abstract

A quiescent prominence was observed at the northwest limb of the Sun using different channels of the Atmospheric Imaging Assembly on board the *Solar Dynamics Observatory*. We report and analyze twisting/swirling motions during and after the prominence eruption. We segregate the observed rotational motions into small and large scales. Small-scale rotational motions manifest in the barbs of the prominence, while the large-scale rotation manifests as the roll motion during the prominence eruption. We noticed that both footpoints of the prominence rotate in the counterclockwise direction. We propose that a similar sense of rotation in both footpoints leads to a prominence eruption. The prominence erupted asymmetrically near the southern footpoint, which may be due to an uneven mass distribution and location of the cavity near the southern footpoint. Furthermore, we study the swirling motion of the plasma along different circular paths in the cavity of the prominence after the prominence eruption. The rotational velocities of the plasma moving along different circular paths are estimated to be ∼9–40 km s^{-1}. These swirling motions can be explained in terms of twisted magnetic field lines in the prominence cavity. Finally we observe the twist built up in the prominence, being carried away by the coronal mass ejection, as seen in the Large Angle Spectrometric Coronagraph on board the *Solar and Heliospheric Observatory*.

Key words: Sun: corona – Sun: coronal mass ejections (CMEs) – Sun: filaments, prominences

Supporting material: animations

1. Introduction

Prominences and/or filaments are ubiquitous in the solar corona. They consist of cool plasma that is embedded in the hot corona. The temperature of the prominences can range from 7500 to 9000 K (Labrosse et al. 2010; Mackay et al. 2010; Parenti 2014). They are observed as a bright arcade structure off the limb in chromospheric lines, e.g., Hα (6562.8 Å) or He II (304 Å), whereas they appear dark in hot coronal lines (Fe IX 171 Å, Fe XII 193 Å). On the disk, they appear darker compared to the background due to the presence of plasma absorption processes and are known as filaments (Parenti 2014). Polarimetric measurements reported the strength of the magnetic field of quiescent prominences between 8 and 10 G for filaments (Lin et al. 1998; Casini et al. 2003) and for prominences (Paletou et al. 2001). High-resolution observations in Hα show that prominences have finer thread-like structures (see Lin et al. 2009; Lin 2011, and references therein). Prominences can remain stable for a long time. Depending on different parameters, like the twist in the magnetic field, mass loading, and ambient magnetic field, they become unstable and erupt (Moore & Labonte 1980; Antiochos 1998; Antiochos et al. 1999; Moore et al. 2001).

Swirling motions have been observed in the solar atmosphere. Chromospheric swirls or small-scale magnetic tornadoes have been observed by Wedemeyer-Böhm & Rouppe van der Voort (2009) and Wedemeyer-Böhm et al. (2012). These authors suggested that these swirls provide a channel to transfer energy from the lower to the upper atmosphere. Several giant tornado-like structures (large scales) have also been reported in the solar atmosphere, which are associated with the vertical structure and barbs of prominences/filaments (Li et al. 2012; Su et al. 2012; Wedemeyer et al. 2013). However, there are only a few reports on the estimation of the rotational speed of the plasma associated with giant tornadoes (Li et al. 2012).

A study of a tornado-like prominence from the extreme ultraviolet imaging spectrometer (EIS) on board *Hinode* and the *Solar Dynamics Observatory*/Atmospheric Imaging Assembly (*SDO*/AIA) indicated a rotation of plasma around the tornado axis (Su et al. 2014). A new model of vortex-filament was suggested by Su et al. (2014), according to which the vortex motions twist the magnetic field. The plasma may be transported from the photosphere through this twisted magnetic field. This gives rise to a highly twisted flux-rope (FR) structure, which eventually becomes unstable after a large twist built up (Wedemeyer et al. 2013; Su et al. 2014). Yan et al. (2014) studied the eruption of an active region filament. The twist buildup was found to be enough for kink instability. They also confirmed that the magnetic helicity was transferred from the photosphere to the corona. In addition to the small-scale twisting motions discussed above, large-scale twists (roll motion) are also reported during a prominence eruption (see Panasenco et al. 2013).

Furthermore, prominence eruptions are usually associated with coronal mass ejections (CMEs), which carry plasma and the magnetic field into the heliosphere and are the main source of geomagnetic disturbances (see Parenti 2014; Gopalswamy 2015, and references therein). Erupting prominences form the bright core of a typical three-part CME, along with a bright frontal lobe and a dark cavity (House et al. 1981; Illing & Hundhausen 1985; Chen 2011).

In this article, we study small- and large-scale twisting and swirling motions before, during, and after a prominence eruption. We propose a new scenario for roll motion in the prominence, which leads to a prominence eruption. A dynamical study of such motions shed new light in the understanding of the evolution of the prominence instability and eventual eruption. We observe a unique scenario of an asymmetric prominence eruption and find signatures of twists built up in the prominence being carried away by the CME. This paper is organized as follows. In Sections 2 and 3, we describe the observation of twisting and swirling motions of the prominence as observed through different extreme ultraviolet channels, methods of data analysis, and results. In Section 4, we describe the association of the CME with the erupting prominence, which is followed by discussions and conclusions in Section 5.

2. Data and Analysis

A prominence eruption was observed at the northwest limb of the Sun on 2012 November 26, by AIA (Lemen et al. 2012) on board *SDO* (see Figure 1(a)). We used 304 Å, 171 Å, and 193 Å emission images of AIA for this study. For the dynamical study, we chose a 10 hr time sequence starting from 11:00 UT on 2012 November 26. The time cadence and the spatial resolution of the data are 12 s and 1.5 arcsec, respectively. The standard *aia_prep.pro* routine was used to process the initial level 1.0 data for correction of roll angles and to calibrate the data from different channels to a common center and plate scale. To focus on the twisting and swirling motions, we used one subfield with a 1 hr duration. The subfield, shown as Region of Interest B (ROI B) in Figure 1(d) and centered at (891 arcsec, 487 arcsec), was chosen for the study of swirling motions after the prominence eruption and is described in Section 3.6. This prominence eruption was associated with a CME at a central principal angle, 340° (see Figure 1(b)), as listed in the *Solar and Heliospheric Observatory* (*SOHO*)/Large Angle and Spectrometric Coronagraph (LASCO) CME catalog (Yashiro et al. 2004). The linear speed of the CME was 299 km s^{-1}. The CME first appeared in the LASCO/C2 field of view at 17:48 UT. The core of the CME was rotating counterclockwise (see the animation of Figure 1). Such CMEs are called "cartwheel" CMEs and have been reported in earlier studies (Kliem et al. 2012). We discuss the prominence–CME association in Section 4.

We further processed the AIA images to enhance faint structures at different spatial scales. First, we convolved each image with a low-pass filter (Gaussian kernel) and subtracted the convolved image with the normal intensity image to retain the features that have high spatial frequency. We iterated this process three times to estimate the uncorrelated noise. Then, we subtracted uncorrelated noise from the original image. To enhance the finer structure, we used a normalized multi-Gaussian filter to the filtered image (see Morgan & Druckmüller 2014; Pant et al. 2015). We chose the width of the Gaussian filter to be 21, 41, and 61 pixels. We added Gaussian filtered images of different spatial scales to the original image. The prominence threads and fine structures in the coronal loops were much more clearly visible in the multi-Gaussian filtered images (see Figure 1(d)). Hereafter, all analyses are done using multi-Gaussian filtered images.

3. Observations and Results

The prominence appeared as a dark elongated structure near the active region AR 11616, as seen in AIA 171 Å emission images on 2012 November 23. Without any apparent changes, this on-disk dark elongated structure moved toward the limb. We followed the evolution of the prominence from 09:00 UT 2012 November 25 to 22:00 UT 2012 November 26. As the prominence started rising (09:00 UT 2012 November 26 onward), we focused on the various stages of the prominence eruption. In the following subsection, we will describe this time evolution in a sequential manner.

3.1. Evolution of the Prominence from 09:00 UT 2012 November 25 to 09:00 UT 2012 November 26

We note that at around 09:00 UT 2012 November 25 near the limb, the prominence barb consisted of three small, dark vertical funnel-like structures (see Figure 2). Overlaying loops (both closed and open) were present in the background. As the filament barbs moved toward the limb, the spine of the filament became visible. The spine consisted of many intertwined and spiraled finer dark threads. The evolution can be seen in the animation of Figure 2.

3.2. Prominence Liftoff and the Eruption (09:00 UT–16:00 UT 2012 November 26)

After 13:00 UT 2012 November 26, the background loops seen in AIA 171 Å disappeared and expanded, which opened the overlaying cavity (middle right panel of Figure 3 and see the animation of Figure 4). As the prominence rose, it twisted and finally erupted around 16:00 UT 2012 November 26. The evolution, as seen by different channels of the AIA, is described below.

The prominence was visible in the AIA 304 Å channel as a bright structure (bottom panels of Figure 3 and the animation of Figure 5) that appears to consist of many dark winding threads in the hotter AIA 171 Å channel (middle panels of Figure 3). Around 11:00 UT, the prominence started rising slowly. The background loops, as seen in AIA 171 Å, disappeared at 13:15 UT (the right middle panel of Figure 3), and subsequently the prominence started rising at a faster pace. After 15:30 UT, during the fast rise, the entire southern footpoint started rotating around a common axis, while the northern footpoint of the prominence rose without any apparent twist. The prominence erupted and the prominence spine broke asymmetrically near the southern footpoint around 16:00 UT. Soon after the eruption, prominence material started falling along twisted paths. After the prominence eruption (after 16:00 UT), we observed swirling motions near the southern footpoint. The entire evolution of the prominence in AIA 171 and 304 Å can be seen in the animations of Figures 4 and 5, respectively.

The evolution of the prominence in AIA 193 Å is the same as observed in the AIA 171 Å channel, except the evolution of the background loops (top panels of Figure 3). The background loops seen in AIA 171 Å disappeared as the prominence started rising up, but the background loops seen in AIA 193 Å did not disappear but appeared to be expanded before and during the prominence eruption (top right panel of Figure 3).

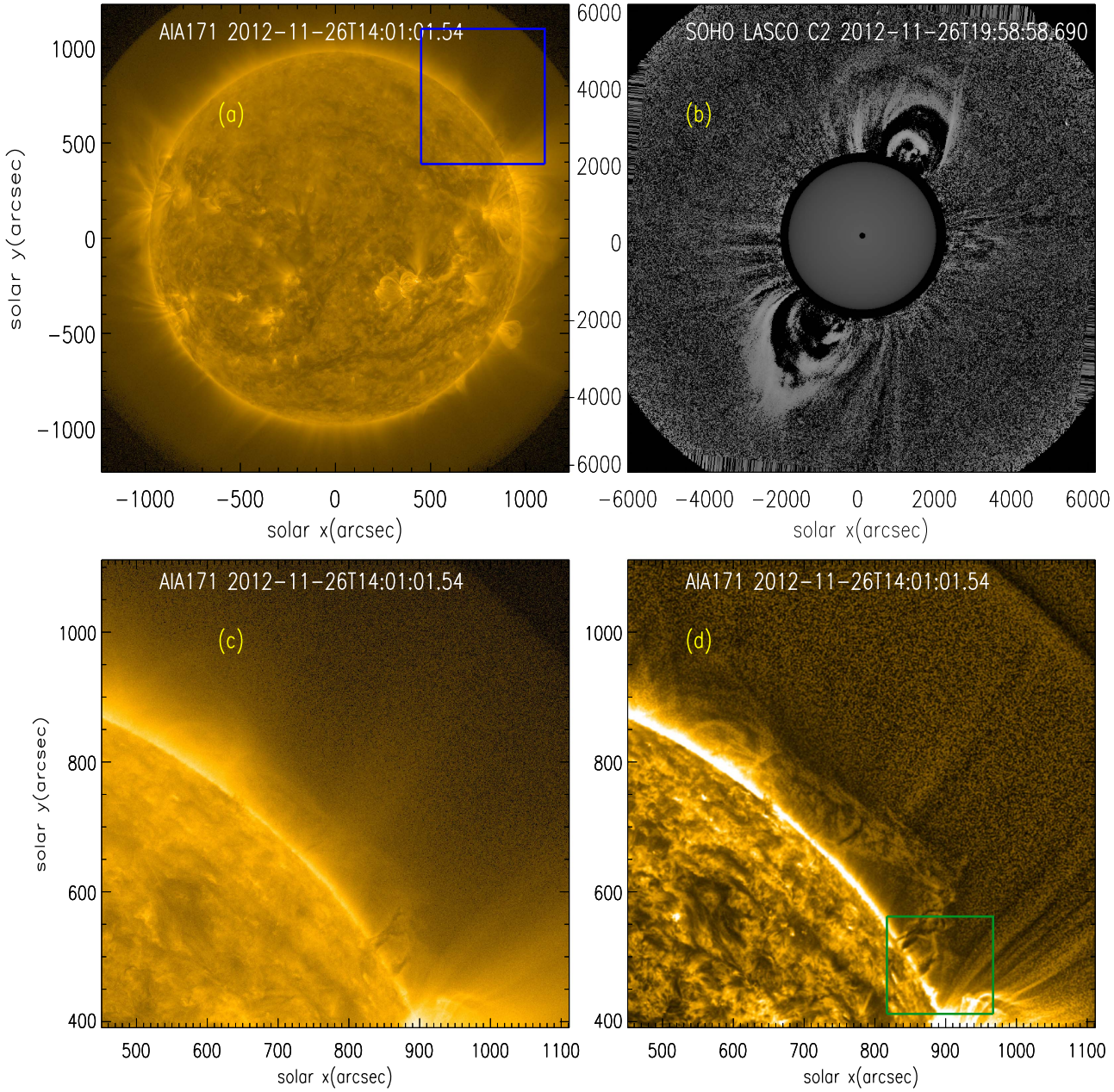

Figure 1. (a) AIA 171 Å full disk image, and the blue rectangle represents Region of Interest A (ROI A). (b) A CME that is associated with the prominence. (c) An AIA 171 Å image of the ROI A. (d) The ROI after applying the multi-Gaussian normalized filter. Twisting and swirling are observed in the region marked by the green rectangle (ROI B).

(An animation of this figure is available.)

3.3. Small-scale Twist of the Prominence Footpoint (11:00 UT–15:00 UT 2012 November 26)

In this subsection, the small-scale twisting motions are described. During the initial rising phase of the prominence, the twisting of individual dark funnels close to the southern footpoint is clearly seen in AIA 171 Å. It is worth noting that the southern footpoint, where the tornado-like structures and twisting motions are seen, is located near the active region, while the northern footpoint is anchored at a quiet region of the Sun, with no apparent twist (see the animation of Figure 4).

Three vertical dark funnels were visible in AIA 171 Å around 11:00 UT at the southern footpoint (Figure 6(a)). During the next one hour, these dark funnels continued to rise slowly. Neither the rotation of the funnels around a certain axis nor the rotation of the funnels themselves are clear from the images (see animated Figure 4). Around 12:00 UT, one of the funnels (f1 in Figure 6(b)) divided into subbranches. The length of the funnels along with the distance between the subbranches increased with time. Around 13:15 UT, the twist was prominent along f1 (Figure 6(c)). This corresponds to the start of the slow rise phase of the prominence. As time progressed, the twist increased in the funnels, and around 14:38 UT, apparently f1 got entangled with the adjacent funnel, f2 (see the zoomed view of Figure 6(d)). Subsequently after 15:00 UT, the fast-rise phase of the prominence started.

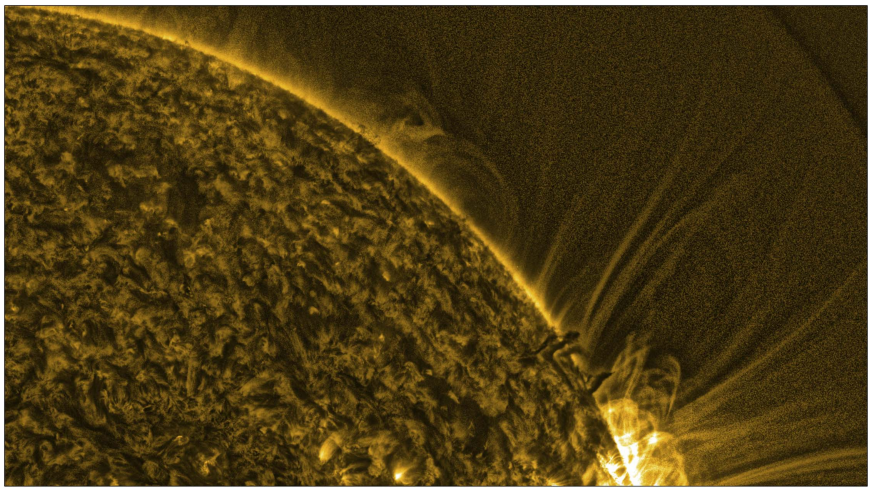

Figure 2. Animation corresponding to this figure shows the evolution of the prominence eruption in the AIA 171 Å channel from 09:00 UT 2012 November 25 to 09:00 UT 2012 November 26.

(An animation of this figure is available.)

3.4. Roll Motion of the Spine (14:30 UT–17:00 UT 2012 November 26)

In this subsection, we present the observation of the large-scale twisting motion, i.e., roll motion, during the prominence eruption.

As the prominence started rising after 13:00 UT, the footpoints (especially the southern footpoint) started rotating as a whole, twisting the prominence spine gradually. The roll motion is visible in AIA 304, 171, and 193 Å channels (see the animations of Figures 4, 5, and 7). The counterclockwise motions of the footpoints are seen in the difference images, as shown in Figure 8. In the top panels of Figure 8, we follow a loop (marked by dotted line) of the southern footpoint before the eruption. Since AIA 304 Å is an optically thick line, we can assume the observed loop in the foreground. Thus the rotation of this loop from north to south indicates that the southern footpoint rotated counterclockwise from the top of view at the local frame. The bright loops associated with the northern footpoint also moved from north to south, as shown in the snapshots of the middle panels. Since these loops are also in the foreground, we concluded that the northern footpoint of the prominence was also twisting counterclockwise.

After the eruption, a swirling motion was observed near the southern footpoint (ROI B). We follow two plasma blobs, marked by violet and blue arrows (bottom panels of Figure 8), as they move along different helical paths. The blobs also show a counterclockwise rotation of the plasma in the plane of the sky. It allows us to interpret that a similar twist might have been built before the eruption.

3.5. Asymmetric Eruption (∼17:00 UT 2012 November 26)

The counterclockwise twist associated with both of the footpoints in turn twisted the spine, and around 17:00 UT, the spine broke asymmetrically near the southern footpoint (see the animations of Figures 4, 5, and 7). We recall that the cavity opened near the southern footpoint (Figure 3) and dark funnels of cool plasma were also present near the southern footpoint only. The opening of the background field lines and uneven distribution of prominence material (densely distributed near the southern footpoint) might have caused the asymmetric eruption of the prominence near the southern footpoint of the prominence.

3.6. Swirling Motion after the Eruption (after 17:30 UT 2012 November 26)

Subsequently around 17:30 UT, a swirling motion started close to the southern footpoint (ROI B in Figure 1(d)). The motion is best seen in the AIA 171 Å channel (see the right-hand panel of the animation of Figure 4). We observed a clockwise, as well as counterclockwise, movement on the plane of the sky of the plasma along different circular paths (Figure 9(a)). We chose two curved slits, namely A and B, along outer channels and another curved slit, C, that is closer to the axis of the swirling structure, as shown in Figure 9(b), to study the swirls. Four-minute running difference images of the spacetime maps along these channels exhibit bright and dark ridges (Figures 9(c)–(e)). Bright ridges with negative (positive) slope indicate plasma movement in the counterclockwise (clockwise) direction. The plasma speeds are estimated from the slopes of the bright ridges of the spacetime maps. Corresponding to the slit location A, we observed counterclockwise motions of plasma with speeds of ∼35–60 km s^{-1}, whereas for B and C locations, both counterclockwise and clockwise movements were recorded. It appears that the plasma follows the helical or twisted field lines, which look like swirling motions. At a later time, the magnetic field lines relaxed and the spiral structure was no longer present.

4. Prominence Eruption and Onset of "Cartwheel" CME

In this section, we will study the properties of the CME associated with the prominence eruption. Although most of the prominence material fell back, a part of it was carried away by the CME. We observe that the twist that was built up around the southern footpoint of the prominence manifested as counterclockwise rotation (see the animation of Figure 1) of the core of the CME. It should be noted that due to the spatial gap between the field of views of AIA and LASCO, a spatial relationship between the twist in the prominence and the rotation of the CME could not be established. The outward propagation of the CME along with the rotation was difficult to

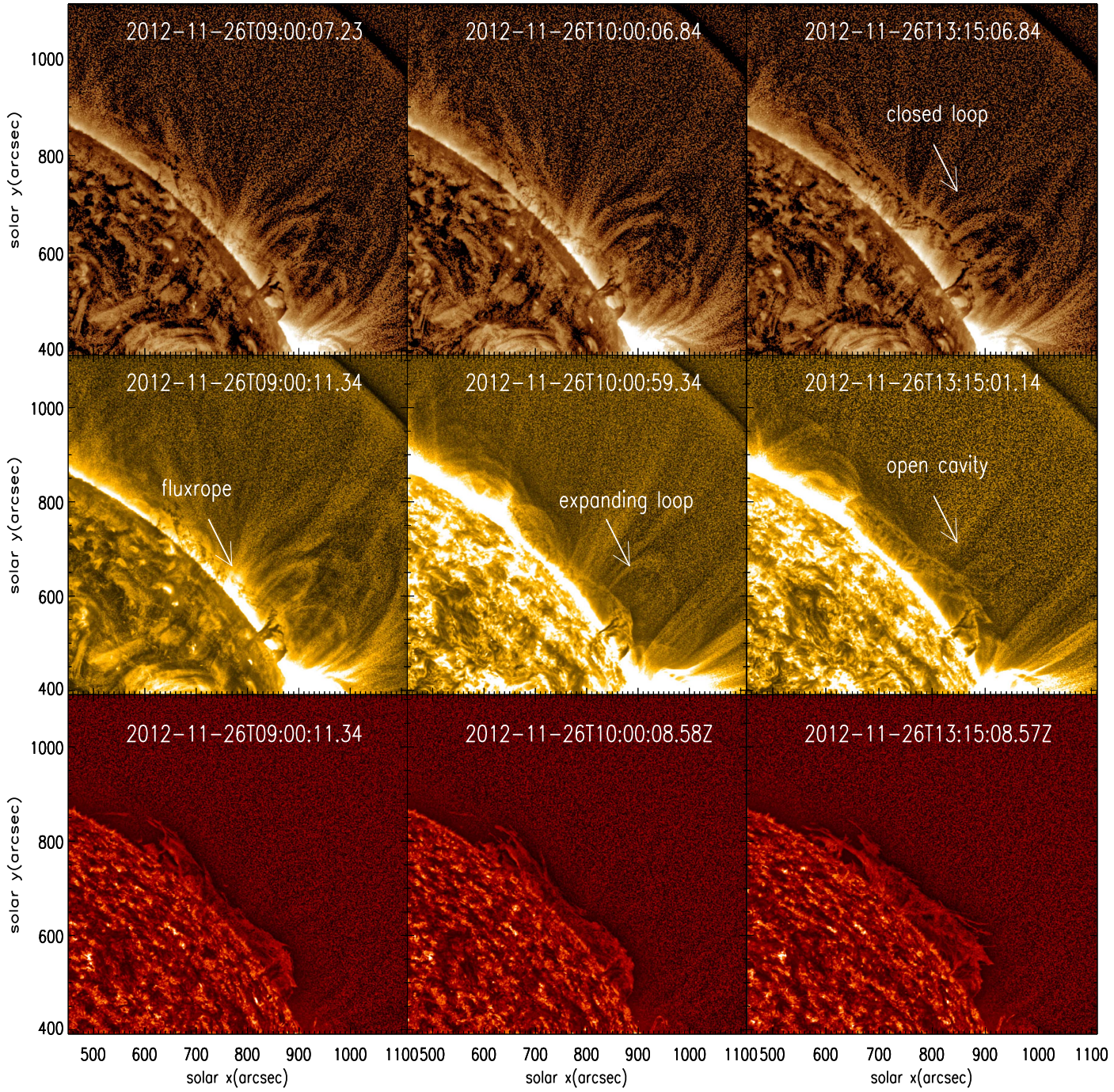

Figure 3. (Top panels) Prominence liftoff and evolution of background loops, as seen by the AIA 193 Å channel. (Middle panels) Same event observed in AIA 171 Å and (bottom panels) AIA 304 Å channels.

capture with the low cadence (12 minutes) of LASCO/C2. Thus we try to estimate the degree of rotation of the features in the CME by tracking some of the prominent features. In order to estimate the degree of rotation, first we choose a feature that was found to be rotating clearly in the coronagraph images. Then the angular position of the feature was calculated. To estimate the angular position of the feature, a circle is fitted such that it passes through the points selected from the bright feature. The angular position is the angle that the feature makes with the horizontal direction. In subsequent images, as the CME moved outward, we estimate the angular position of the feature at every frame. Therefore, as the feature rotated, the angular position changed. We track the feature until it either disappeared from the coronagraph images or became too faint to be detected. We apply this procedure to two features identified in the coronagraph images (see Figures 10 and 11) and note that they rotated by 150° and 64°, respectively. First feature appeared at 19:00 UT and disappeared after 20:24 UT, while the second feature appeared at 20:48 UT. Therefore, the total degree of rotation is the sum of the degree of rotation of both features, i.e., 214°, assuming that these two features were the part of the same prominence. It should be noted that the

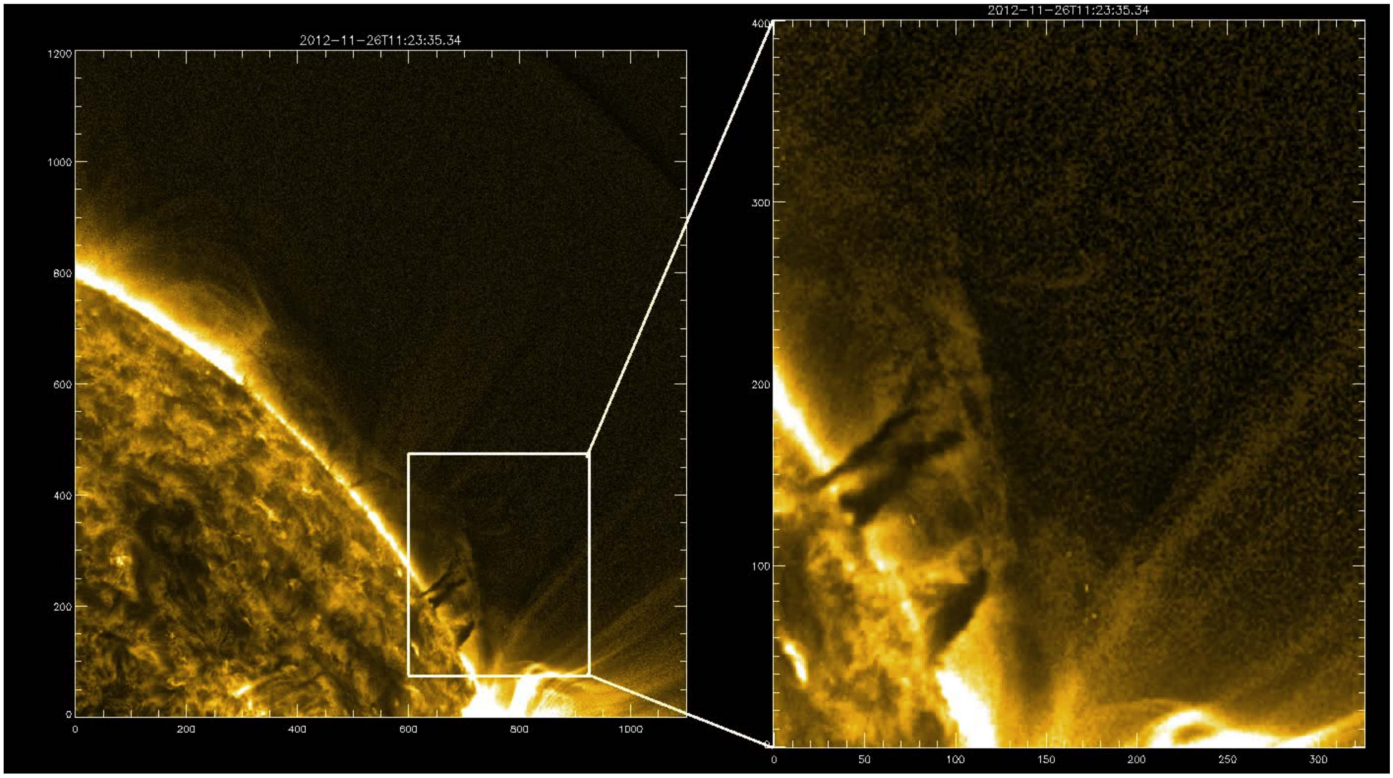

Figure 4. Animation corresponding to this figure shows the evolution of the prominence eruption in the AIA 171 Å channel from 09:00 UT to 18:00 UT 2012 November 26. Right panel shows the zoomed view of the vertical funnels/tornadoes.

(An animation of this figure is available.)

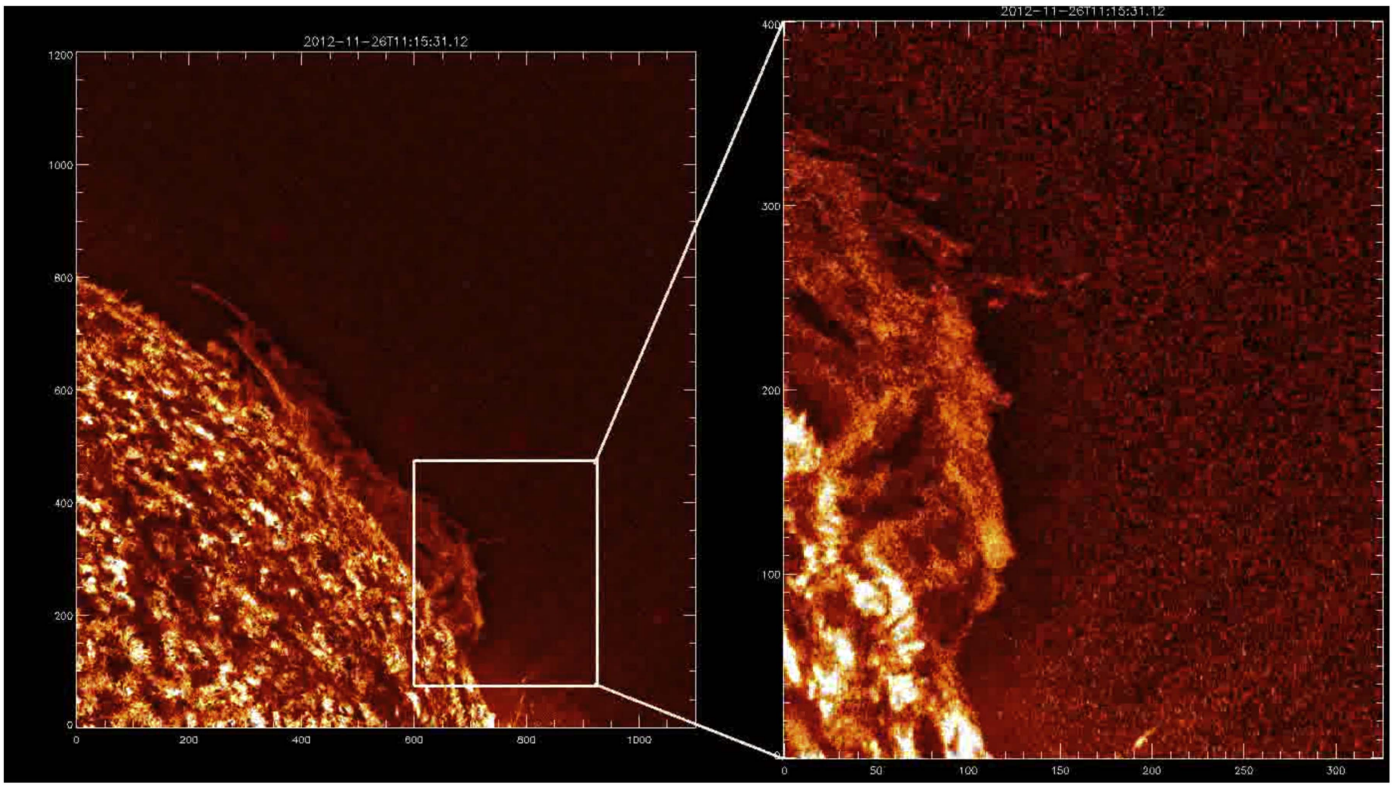

Figure 5. Same as in Figure 4 but for the AIA 304 Å channel.

(An animation of this figure is available.)

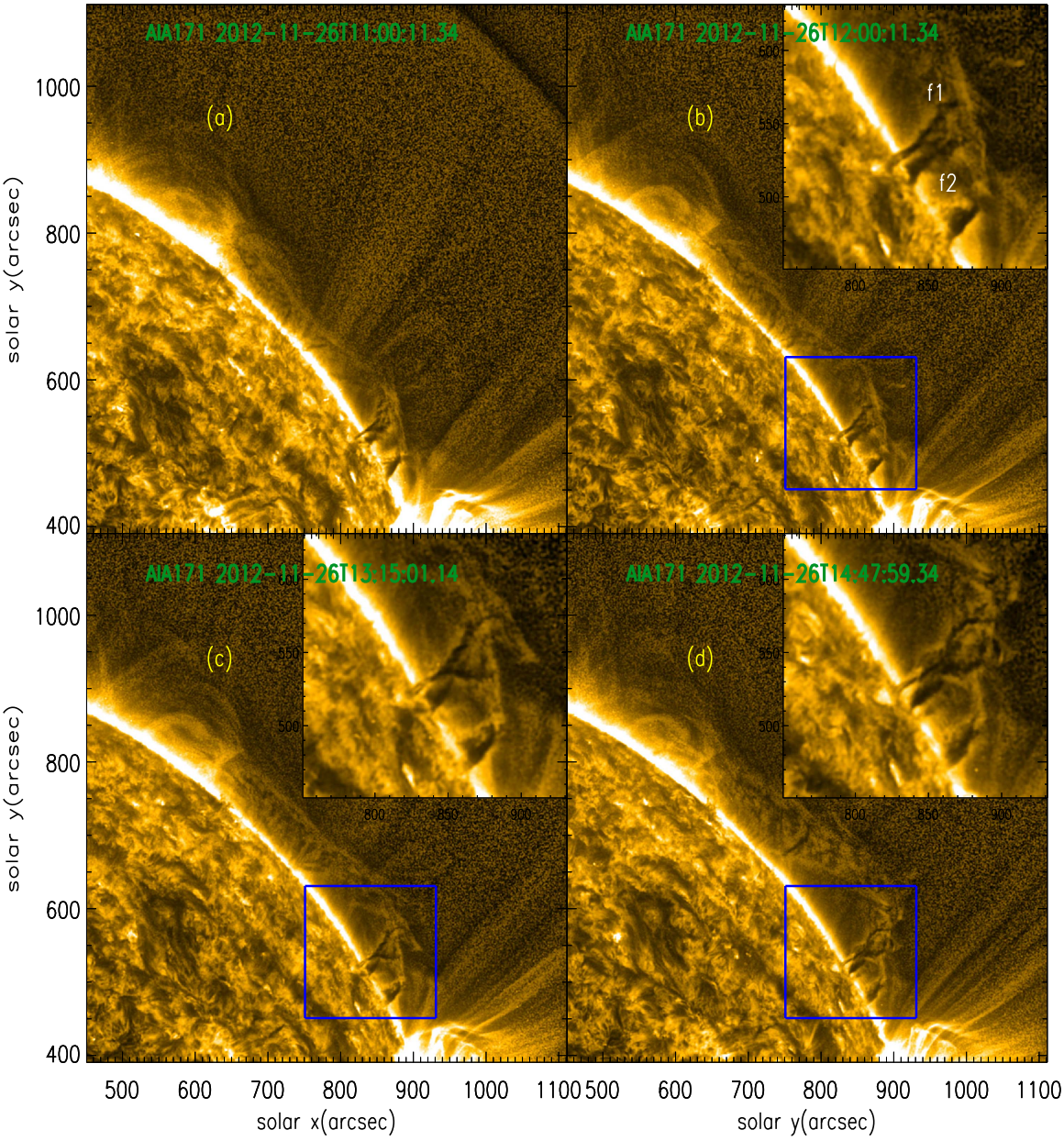

Figure 6. Rising phase of the prominence along with the twist in the southern footpoint, as seen in the AIA 171 Å channel. The vertical dark funnels near the southern footpoint twist during the rising phase. The blue rectangles in panels (b)–(d) indicate the zoomed area shown in the corner of the corresponding panels. The dark funnels twist, branch, and entangle as they continue to rise. Note that the region enclosed in the blue box is different from ROI B.

degree of rotation will not be affected by the projection in the plane of sky. This is still an underestimate of the total twist because we could not see clear features in all frames.

5. Discussions and Conclusions

In this paper, we study a dynamical evolution of a quiescent prominence eruption, which includes twisting, swirling motions, and an association with a CME. Here we summarize the different stages of the evolution of the prominence eruption and salient features associated with it.

We found that the overlying loops, as seen in AIA 171 Å, disappeared prior to the prominence liftoff, and as expected, subsequently the prominence erupted. However, neither the signature of the FR nor the background loops were seen in hotter channels of AIA, 94 and 335 Å. We considered barbs as rotating funnel-like structures. Since the length scale of the rotation in barbs is small as compared to the roll motion of the prominence, we termed the rotation of barbs as small-scale twisting motion. Such rotating structures have been termed giant tornadoes by Wedemeyer et al. (2013). The southern footpoint of the prominence was lying in close proximity to the active region. Photospheric vortex flows are more frequent near the active region (Bello González et al. 2012; Dhara et al. 2014), thus it may explain why the southern footpoint manifested a larger twist as compared to the northern footpoint, which was anchored at the quiet region of the Sun. However, it should be noted that the photospheric vortex motions cannot be measured because the footpoints of the prominence were at the limb. Furthermore, the rotation of the tornado could transfer cool material and a magnetic twist to upper layers. The magnetic twist increased the coronal

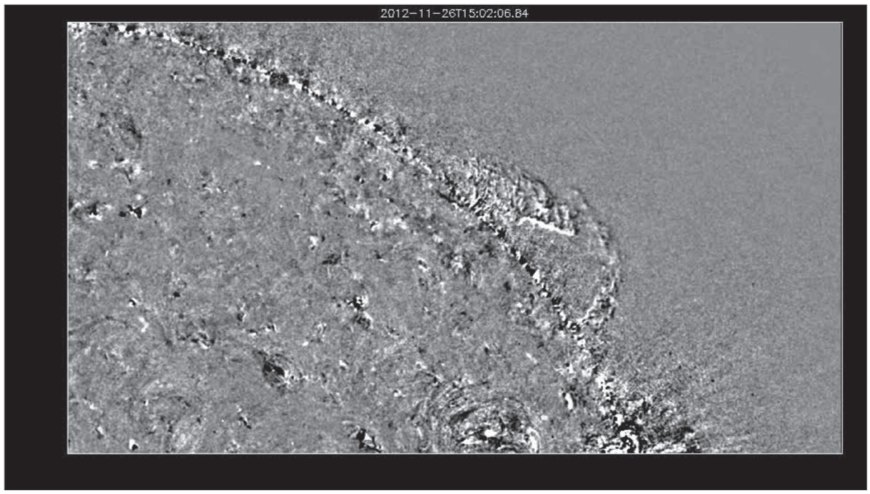

Figure 7. Animation corresponding to this figure represents the difference image of AIA 193 Å. Roll motion is clearly seen in the difference image. (An animation of this figure is available.)

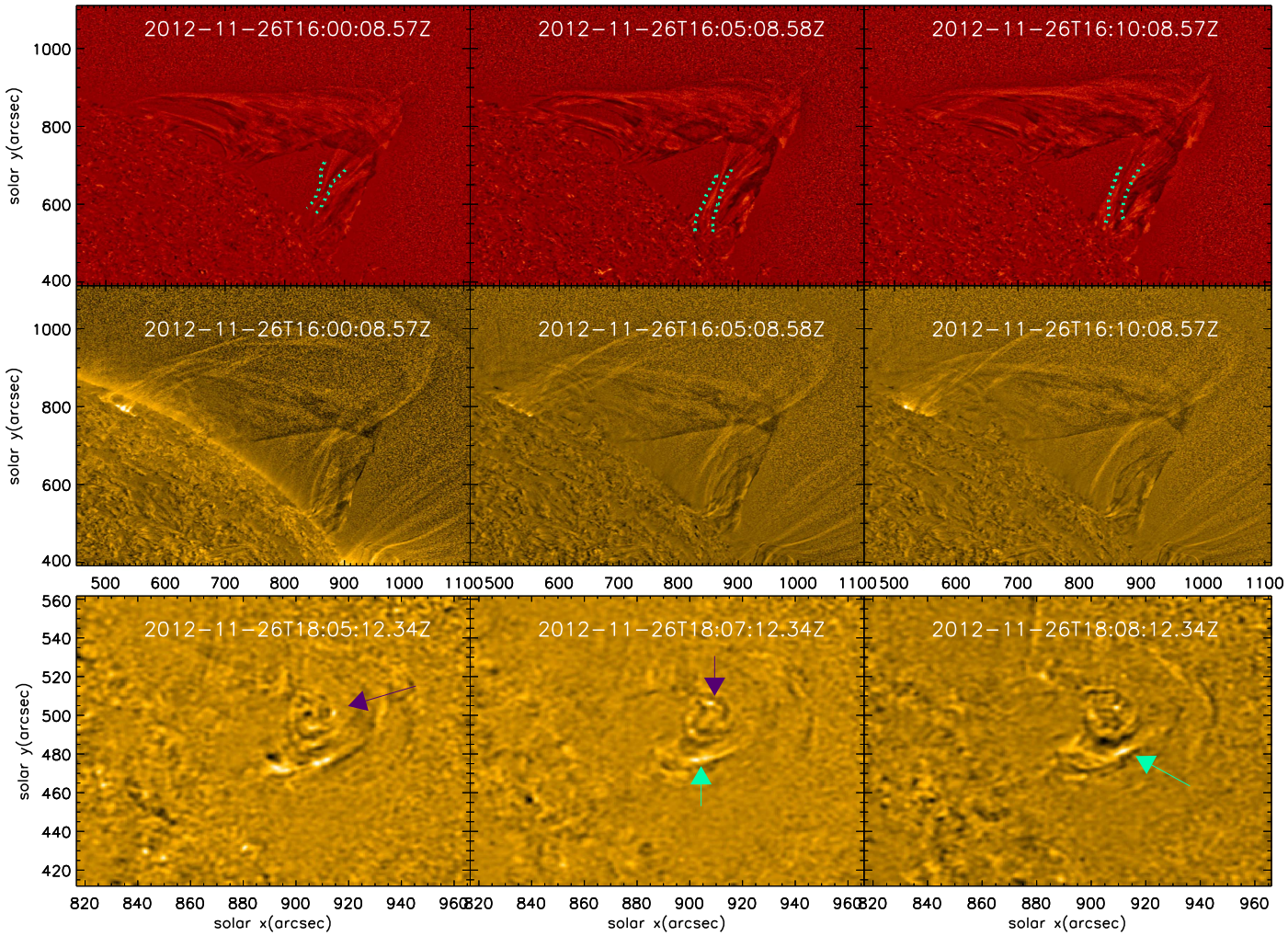

Figure 8. (Top panels) Difference images before the eruption in the AIA 304 Å channel showing counterclockwise rotation. Dashed lines show the positions of a foreground loop at the southern footpoint in consecutive snapshots. (Middle panels) Counterclockwise rotation of the northern footpoint before the eruption, as seen in AIA 171 Å difference images. (Bottom panels) Swirling motion of the southern footpoint after the eruption in the AIA 171 Å channel. Tracked features are marked with arrows in the consecutive snapshots.

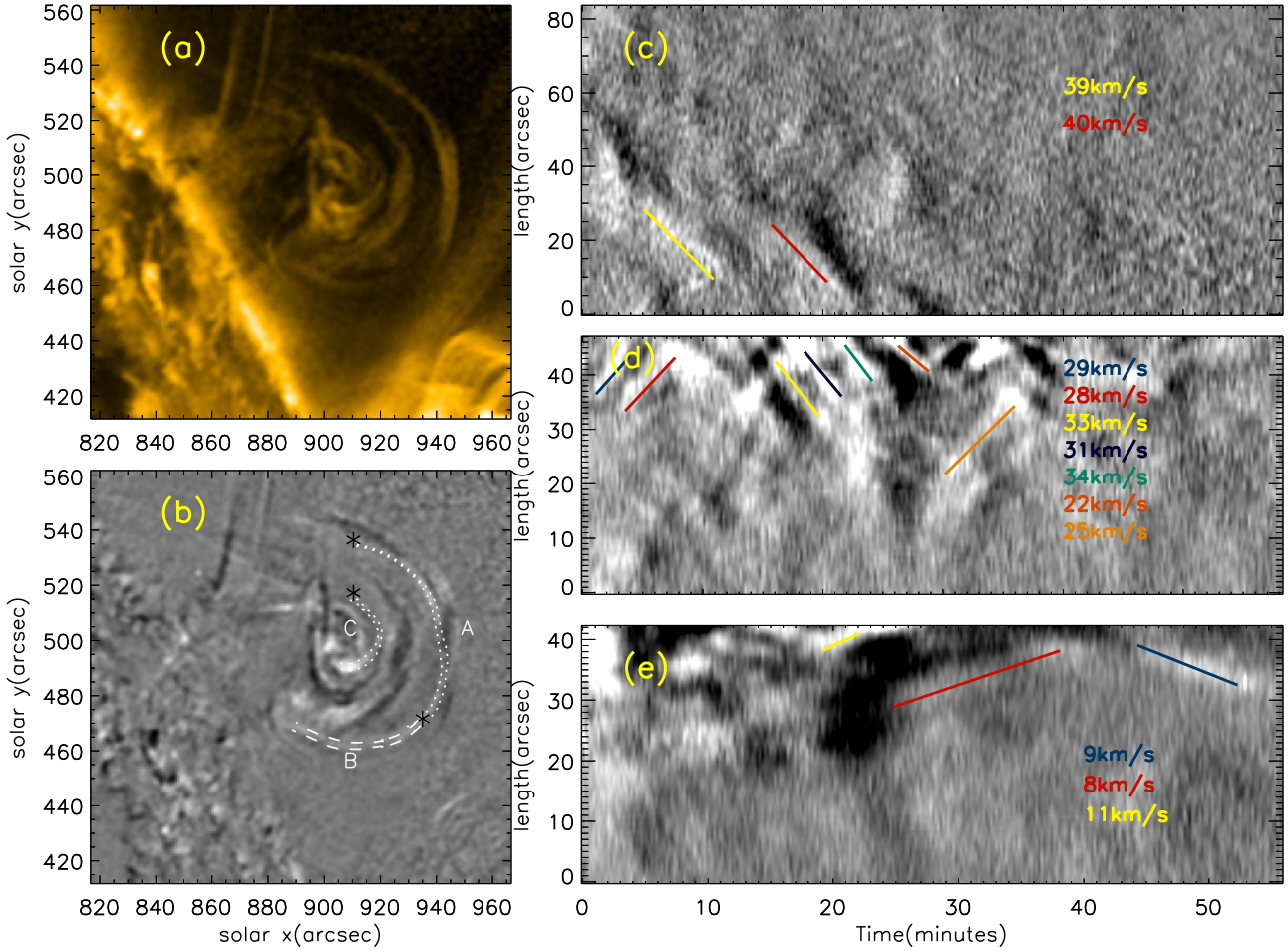

Figure 9. (a) Tornado-like swirl near the right footpoint, as seen in the AIA 171 Å channel (ROI B in Figure 1 (d)). (b) Running difference image of the same region. Curved slits A, B, and C are used to study the plasma movement during the swirl. The zero in the y-axis in the spacetime maps presented in panels (c)–(e) are denoted by a "star" symbol. (c)–(e) Running difference images of spacetime maps from curved slits A, B, and C, respectively. Speeds of plasma movement through different channels are calculated from the slope of the bright ridges. The positive and negative slopes corresponds to the clockwise and counterclockwise rotation along the slit.

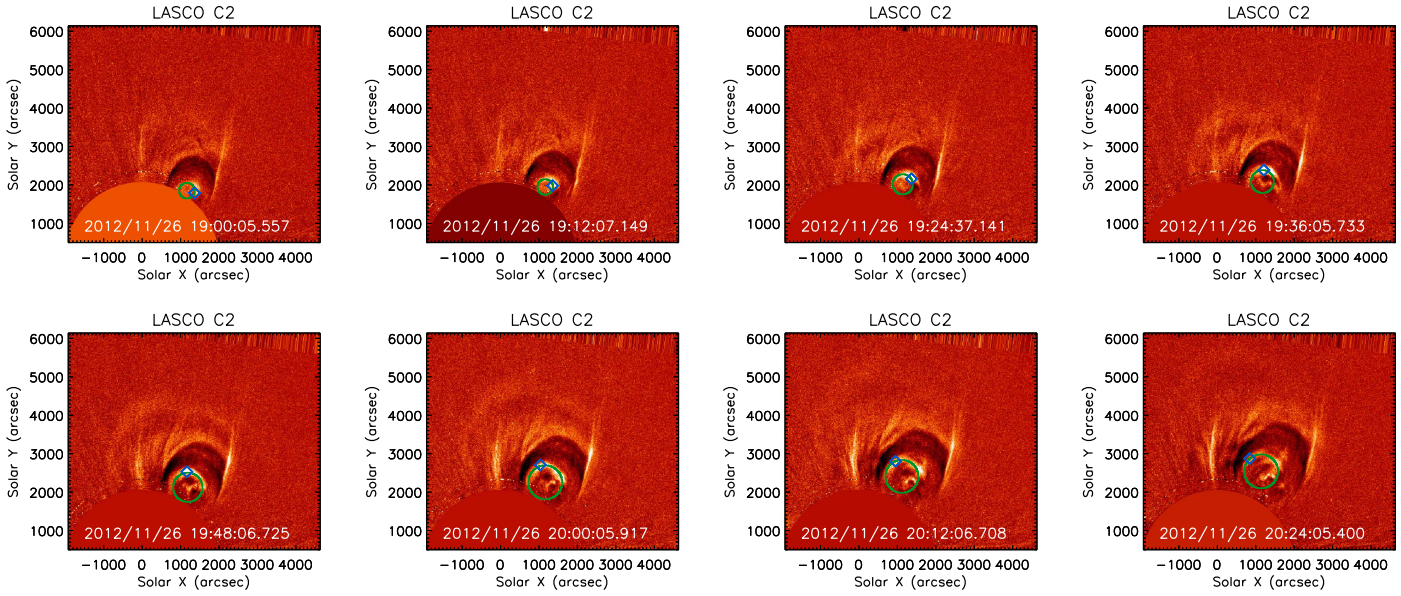

Figure 10. LASCO/C2 running difference image. Blue diamonds represent the feature that is rotating counterclockwise. Since the feature is extended, the diamond symbol represents the location of maximum brightness. Green circles pass through the feature of interest and are used to estimate the angular position of the feature. The degree of rotation is 150°.

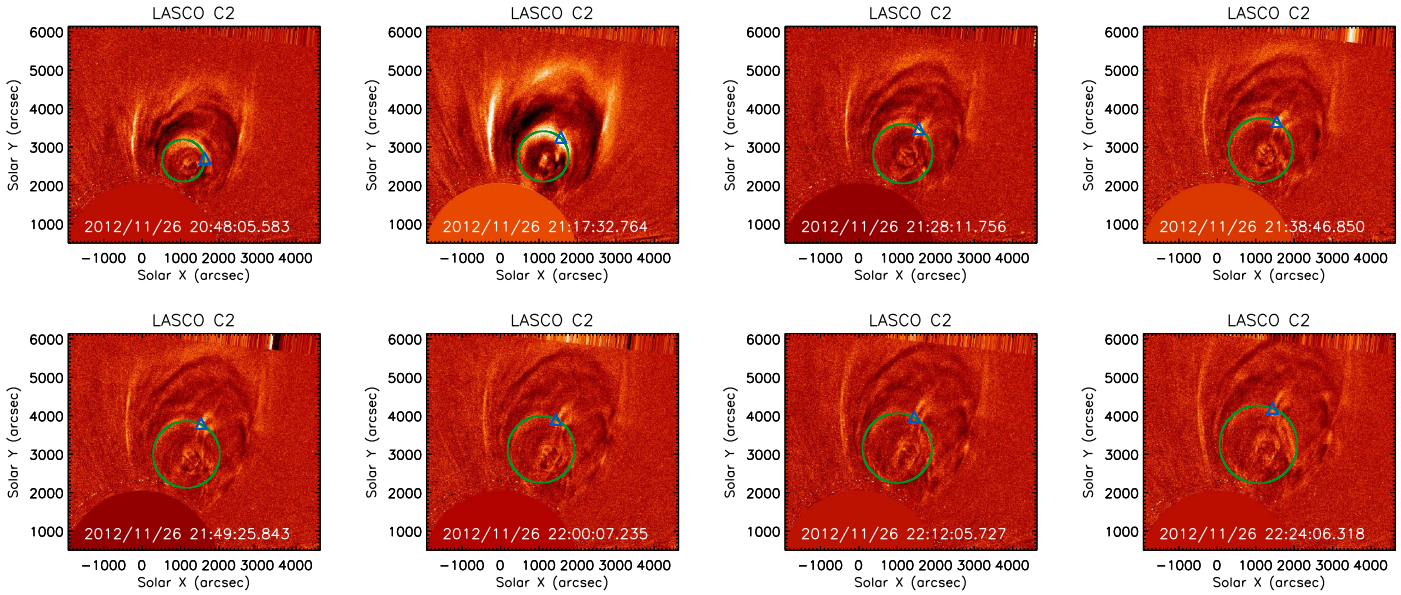

Figure 11. Same as in Figure 10, except for a different feature marked with a blue triangle. The degree of rotation is 64°.

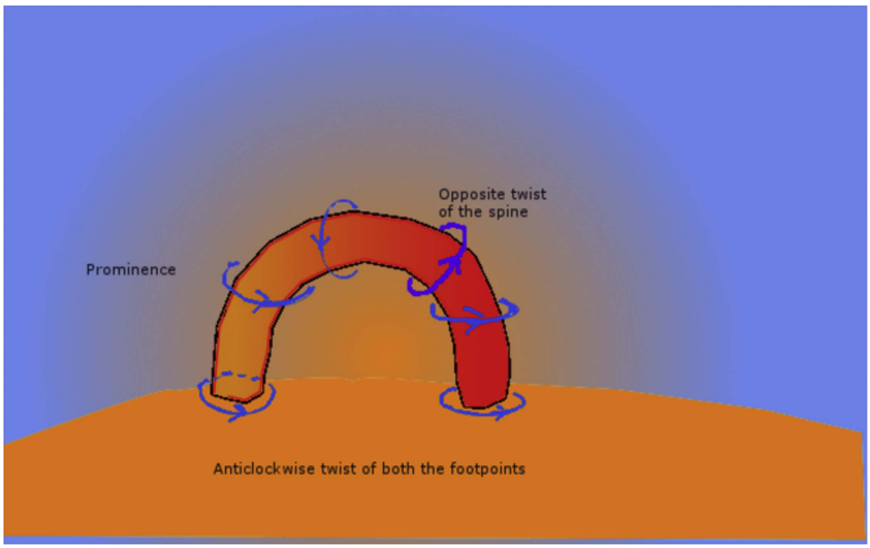

Figure 12. Cartoon showing the twist at both footpoints of the prominence in the same direction. When the twist propagates upward, it twists two sides of the spine of the prominence in opposite directions, which causes the prominence spine to break.

magnetic field stress, and the prominence became unstable. This scenario is consistent with Su et al. (2014).

In contrast to Panasenco et al. (2013), we observed that the twist in both footpoints of the prominence was counterclockwise. We describe this scenario with a cartoon shown in Figure 12, where we have shown that the counterclockwise twist of the two footpoints results in the opposite twist at the spine of the prominence that leads to the prominence eruption. This is the main finding from our study. To our knowledge, this scenario has not been reported earlier. We noted that the prominence erupted asymmetrically near the southern footpoint. Several factors may contribute to the asymmetric eruption. First, we found the signatures of the expanding cavity above the prominence in AIA 171 and 193 Å images. From Figure 3, we noted that the magnetic field configuration was different over two footpoints of the prominence. The cavity was located near the southern footpoint, and we observed that the prominence started rising at the location of the open cavity. We have not observed any signatures of possible reconnection during this event. So the reason behind the change in the magnetic topology is not clear to us. Second, we believe that the prominence material was densely distributed at the southern footpoint due to the presence of dark funnel-like structures. Uneven distribution of the prominence material and the open cavity located near the southern footpoint facilitated the easy liftoff of the prominence near the southern footpoint. This scenario of the asymmetric eruption of the prominence is also a new result that has not been reported earlier.

We noted the swirling motion of the plasma along several circular paths after the prominence eruption. It appears that the swirling motion was caused by the falling material along the helical field lines that were located around the dark funnels/tornadoes. This is consistent with the numerical model of Xia et al. (2014). The authors have simulated the condensation process in a solar prominence, with the helical field lines in the

cavity of the prominence (see Figure 5 of Xia et al. 2014). After the eruption, the plasma blobs may follow these helical field lines and cause swirling motions. We conjecture that the helical field lines might have resulted from the twist that was built up around the southern footpoint of the prominence. Finally these helical field lines might have disappeared, and the shape might have completely changed, which could explain the disappearance of the dark funnels/tornadoes and the spiral structure. Furthermore, we found that a part of the twist was also carried away by the CME associated with the prominence eruption. We estimated the degree of rotation to be $\sim 214^{\circ}$ at ~ 3 solar radii. Such a high degree of rotation has not been reported in earlier studies. A similar event, nicknamed the "cartwheel CME," was observed by Thompson et al. (2012) and Patsourakos & Vourlidas (2011). A rotation of 115° was estimated at 2.5 solar radii, which is much less than the degree of rotation reported in this study.

The study of the rotation is important to understand the eruption mechanism of the FR (Kliem et al. 2012). For instance, the rotation of the FR and the associated CME may indicate the occurrence of helical Kink Instability (KI; Kliem et al. 2012). Kliem et al. (2012) performed numerical simulations of a "cartwheel" CME that resulted from an erupting FR. In the numerical model, they used external toroidal field component pointing along the FR. They proposed that the rotation by KI depends on the initial twist in the FR, the strength, and the height profile of the overlying field. If the overlying field decreases slowly with height, then the rotation will be strong at small heights. Otherwise, the rotation will be distributed over large heights. They tried to fit the observations by varying the strength of the external toroidal field (sheer field) and the initial twist in the FR. Thus the degree of rotation provides strong constraints for the numerical modeling. The authors also proposed that the twist in an FR (5π) alone is not enough to match the rotational profile. The inclusion of the external sheer field is required to match the observed rotation. Thus the degree of rotation of a CME may be used to probe the magnetic field topology of the overlying field and its variation with height by performing numerical modeling similar to Kliem et al. (2012). The high degree of rotation observed in this study may provide strong constraints on the existing models. We conjecture that the high degree of rotation may happen due to the highly sheared external magnetic field.

Thus we conclude that the small-scale twist of dark funnels/tornadoes present near the southern footpoint might be responsible for the large-scale twist in the footpoints of the prominence (roll motion) during the prominence eruption. A similar sense of rotation in both footpoints of the prominence caused the prominence spine to break, which led to the prominence eruption. The counterclockwise rotation at the footpoints of the prominence manifested as rotating features inside the CME. Thus we feel that this morphological study of a prominence eruption may provide new insight into the prominence eruption models. However, further studies with better quantitative estimates are needed to confirm some of the findings reported here.

Authors thank anonymous referee for the valuable comments that have helped us to substantially improve the manuscript. The authors would also like to thank Yingna Su for her constructive comments. AIA/*SDO* data are provided by the Joint Science Operations Center Science Data Processing. The *SDO* data used are the courtesy of NASA/*SDO* and the AIA, EVE, and HMI science teams.

ORCID iDs

V. Pant https://orcid.org/0000-0002-6954-2276
A. Datta https://orcid.org/0000-0003-4176-128X
D. Banerjee https://orcid.org/0000-0003-4653-6823

References

Antiochos, S. K. 1998, ApJL, 502, L181
Antiochos, S. K., DeVore, C. R., & Klimchuk, J. A. 1999, ApJ, 510, 485
Bello González, N., Kneer, F., & Schlichenmaier, R. 2012, A&A, 538, A62
Casini, R., López Ariste, A., Tomczyk, S., & Lites, B. W. 2003, ApJL, 598, L67
Chen, P. F. 2011, LRSP, 8, 1
Dhara, S. K., Ravindra, B., & Banyal, R. K. 2014, SoPh, 289, 4481
Gopalswamy, N. 2015, in Solar Prominences, Astrophysics and Space Science Library Vol. 415, ed. J.-C. Vial & O. Engvold (Cham: Springer), 381
House, L. L., Wagner, W. J., Hildner, E., Sawyer, C., & Schmidt, H. U. 1981, ApJL, 244, L117
Illing, R. M. E., & Hundhausen, A. J. 1985, JGR, 90, 275
Kliem, B., Török, T., & Thompson, W. T. 2012, SoPh, 281, 137
Labrosse, N., Heinzel, P., Vial, J.-C., et al. 2010, SSRv, 151, 243
Lemen, J. R., Title, A. M., Akin, D. J., et al. 2012, SoPh, 275, 17
Li, X., Morgan, H., Leonard, D., & Jeska, L. 2012, ApJL, 752, L22
Lin, H., Penn, M. J., & Kuhn, J. R. 1998, ApJ, 493, 978
Lin, Y. 2011, SSRv, 158, 237
Lin, Y., Soler, R., Engvold, O., et al. 2009, ApJ, 704, 870
Mackay, D. H., Karpen, J. T., Ballester, J. L., Schmieder, B., & Aulanier, G. 2010, SSRv, 151, 333
Moore, R. L., & Labonte, B. J. 1980, in IAU Symp. 91, Solar and Interplanetary Dynamics, ed. M. Dryer & E. Tandberg-Hanssen (Dordrecht: Reidel), 207
Moore, R. L., Sterling, A. C., Hudson, H. S., & Lemen, J. R. 2001, ApJ, 552, 833
Morgan, H., & Druckmüller, M. 2014, SoPh, 289, 2945
Paletou, F., López Ariste, A., Bommier, V., & Semel, M. 2001, A&A, 375, L39
Panasenco, O., Martin, S. F., Velli, M., & Vourlidas, A. 2013, SoPh, 287, 391
Pant, V., Datta, A., & Banerjee, D. 2015, ApJL, 801, L2
Parenti, S. 2014, LRSP, 11, 1
Patsourakos, S., & Vourlidas, A. 2011, A&A, 525, A27
Su, Y., Gömöry, P., Veronig, A., et al. 2014, ApJL, 785, L2
Su, Y., Wang, T., Veronig, A., Temmer, M., & Gan, W. 2012, ApJL, 756, L41
Thompson, W. T., Kliem, B., & Török, T. 2012, SoPh, 276, 241
Wedemeyer, S., Scullion, E., Rouppe van der Voort, L., Bosnjak, A., & Antolin, P. 2013, ApJ, 774, 123
Wedemeyer-Böhm, S., & Rouppe van der Voort, L. 2009, A&A, 507, L9
Wedemeyer-Böhm, S., Scullion, E., Steiner, O., et al. 2012, Natur, 486, 505
Xia, C., Keppens, R., Antolin, P., & Porth, O. 2014, ApJL, 792, L38
Yan, X. L., Xue, Z. K., Liu, J. H., Kong, D. F., & Xu, C. L. 2014, ApJ, 797, 52
Yashiro, S., Gopalswamy, N., Michalek, G., et al. 2004, JGRA, 109, A07105